Polarization-sensitive spectral-domain optical coherence tomography using a single line scan camera

Cense, B.; Mujat, M.; Chen, T.; Park, B. H.; de Boer, J.F.

published in
Optics Express
2007

DOI (link to publisher)
10.1364/OE.15.002421

document version
Publisher's PDF, also known as Version of record

Polarization-sensitive spectral-domain optical coherence tomography using a single line scan camera

Barry Cense[1] and Mircea Mujat

Harvard Medical School and Wellman Center for Photomedicine, Massachusetts General Hospital, 50 Blossom Street, BAR 7, Boston, Massachusetts 02114

[1]Currently with Indiana University, School of Optometry, 800 E. Atwater Ave, Bloomington, Indiana 47405
bcense@indiana.edu

Teresa C. Chen

Massachusetts Eye and Ear Infirmary and Harvard Medical School, 243 Charles Street, Boston, Massachusetts 02114

B. Hyle Park and Johannes F. de Boer

Harvard Medical School and Wellman Center for Photomedicine, Massachusetts General Hospital, 50 Blossom Street, BAR 7, Boston, Massachusetts 02114
deboer@helix.mgh.harvard.edu

Abstract: Polarization-sensitive optical coherence tomography can be used to measure the birefringence of biological tissue such as the human retina. Previous measurements with a time-domain polarization-sensitive optical coherence tomography system revealed that the birefringence of the human retinal nerve fiber layer is not constant, but varies as a function of location around the optic nerve head. Here we present a spectral-domain polarization-sensitive optical coherence tomography system that uses a spectrometer configuration with a single line scan camera and a Wollaston prism in the detection arm. Since only one camera has to be synchronized with other components in the system, the design is simplified considerably. This system is 60 times faster than a time-domain polarization-sensitive optical coherence tomography system. Data was acquired using concentric circular scans around the optic nerve head of a young healthy volunteer and the acquisition time for 12 circular scans was reduced from 72 s to 1.2 s. The acquired data sets demonstrate variations in retinal thickness and double pass phase retardation per unit depth that were similar to data from the same volunteer taken with a time-domain polarization-sensitive system. The double pass phase retardation per unit depth of the retinal nerve fiber layer varied between 0.18 and 0.40 degrees/μm, equivalent to a birefringence of $2.2 \cdot 10^{-4}$ and $4.8 \cdot 10^{-4}$ respectively, measured at 840 nm.

OCIS codes: (170.4500) Optical Coherence Tomography; (170.4470) Ophthalmology; (170.3890) Medical optics instrumentation.

References and links

1. D. Huang, E.A. Swanson, C.P. Lin, J.S. Schuman, W.G. Stinson, W. Chang, M.R. Hee, T. Flotte, K. Gregory, C.A. Puliafito, and J.G. Fujimoto, "Optical Coherence Tomography," Science **254,** 1178-1181 (1991).
2. A.F. Fercher, C.K. Hitzenberger, G. Kamp, and S.Y. Elzaiat, "Measurement of intraocular distances by backscattering spectral interferometry," Opt. Commun. **117,** 43-48 (1995).

#78463 - $15.00 USD Received 22 December 2006; revised 13 February 2007; accepted 15 February 2007

3. M.R. Hee, D. Huang, E.A. Swanson, and J.G. Fujimoto, "Polarization-sensitive low-coherence reflectometer for birefringence characterization and ranging," J. Opt. Soc. Am. B **9,** 903-908 (1992).
4. J.F. de Boer, T.E. Milner, M.J.C. van Gemert, and J.S. Nelson, "Two-dimensional birefringence imaging in biological tissue by polarization-sensitive optical coherence tomography," Opt. Lett. **22,** 934-936 (1997).
5. J.F. de Boer, T.E. Milner, and J.S. Nelson, "Determination of the depth-resolved Stokes parameters of light backscattered from turbid media by use of polarization-sensitive optical coherence tomography," Opt. Lett. **24,** 300-302 (1999).
6. C.E. Saxer, J.F. de Boer, B.H. Park, Y.H. Zhao, Z.P. Chen, and J.S. Nelson, "High-speed fiber-based polarization-sensitive optical coherence tomography of in vivo human skin," Opt. Lett. **25,** 1355-1357 (2000).
7. S.L. Jiao and L.H.V. Wang, "Jones-matrix imaging of biological tissues with quadruple- channel optical coherence tomography," J. Biomed. Opt. **7,** 350-358 (2002).
8. B. Cense, T.C. Chen, B.H. Park, M.C. Pierce, and J.F. de Boer, "In vivo depth-resolved birefringence measurements of the human retinal nerve fiber layer by polarization-sensitive optical coherence tomography," Opt. Lett. **27,** 1610-1612 (2002).
9. B. Cense, T.C. Chen, B.H. Park, M.C. Pierce, and J.F. de Boer, "Thickness and birefringence of healthy retinal nerve fiber layer tissue measured with polarization-sensitive optical coherence tomography," Invest. Ophthalmol. Vis. Sci. **45,** 2606-2612 (2004).
10. B. Cense, "*Optical coherence tomography for retinal imaging*," PhD thesis, (2005).
11. X.R. Huang, H. Bagga, D.S. Greenfield, and R.W. Knighton, "Variation of peripapillary retinal nerve fiber layer birefringence in normal human subjects," Invest. Ophthalmol. Vis. Sci. **45,** 3073-3080 (2004).
12. X.R. Huang and R.W. Knighton, "Microtubules contribute to the birefringence of the retinal nerve fiber layer," Invest. Ophthalmol. Vis. Sci. **46,** 4588-4593 (2005).
13. M. Wojtkowski, R. Leitgeb, A. Kowalczyk, T. Bajraszewski, and A.F. Fercher, "In vivo human retinal imaging by Fourier domain optical coherence tomography," J. Biomed. Opt. **7,** 457-463 (2002).
14. T. Mitsui, "Dynamic range of optical reflectometry with spectral interferometry," Jpn. J. Appl. Phys. Part 1 - Regul. Pap. Short Notes Rev. Pap. **38,** 6133-6137 (1999).
15. R. Leitgeb, C.K. Hitzenberger, and A.F. Fercher, "Performance of fourier domain vs. time domain optical coherence tomography," Opt. Express **11,** 889-894 (2003).
16. J.F. de Boer, B. Cense, B.H. Park, M.C. Pierce, G.J. Tearney, and B.E. Bouma, "Improved signal-to-noise ratio in spectral-domain compared with time-domain optical coherence tomography," Opt. Lett. **28,** 2067-2069 (2003).
17. M.A. Choma, M.V. Sarunic, C.H. Yang, and J.A. Izatt, "Sensitivity advantage of swept source and Fourier domain optical coherence tomography," Opt. Express **11,** 2183-2189 (2003).
18. Y. Yasuno, S. Makita, Y. Sutoh, M. Itoh, and T. Yatagai, "Birefringence imaging of human skin by polarization-sensitive spectral interferometric optical coherence tomography," Opt. Lett. **27,** 1803-1805 (2002).
19. B.H. Park, M.C. Pierce, B. Cense, S.H. Yun, M. Mujat, G.J. Tearney, B.E. Bouma, and J.F. de Boer, "Real-time fiber-based multi-functional spectral-domain optical coherence tomography at 1.3 mu m," Opt. Express **13,** 3931-3944 (2005).
20. E. Götzinger, M. Pircher, and C.K. Hitzenberger, "High speed spectral domain polarization sensitive optical coherence tomography of the human retina," Opt. Express **13,** 10217-10229 (2005).
21. M. Yamanari, S. Makita, V.D. Madjarova, T. Yatagai, and Y. Yasuno, "Fiber-based polarization-sensitive Fourier domain optical coherence tomography using B-scan-oriented polarization modulation method," Opt. Express **14,** 6502-6515 (2006).
22. N. Nassif, B. Cense, B.H. Park, S.H. Yun, T.C. Chen, B.E. Bouma, G.J. Tearney, and J.F. de Boer, "In vivo human retinal imaging by ultrahigh-speed spectral domain optical coherence tomography," Opt. Lett. **29,** 480-482 (2004).
23. N.A. Nassif, B. Cense, B.H. Park, M.C. Pierce, S.H. Yun, B.E. Bouma, G.J. Tearney, T.C. Chen, and J.F. de Boer, "In vivo high-resolution video-rate spectral-domain optical coherence tomography of the human retina and optic nerve," Opt. Express **12,** 367-376 (2004).
24. A.N.S.I., *Safe use of lasers*. 1993, Laser Institute of America: New York.
25. M. Mujat, B.H. Park, B. Cense, T.C. Chen, and J.F. De Boer, "Auto-calibration of spectral-domain optical coherence tomography spectrometers for in-vivo quantitative retinal nerve fiber layer birefringence determination," J. Biomed. Opt. (Submitted)**,** (2006).
26. M. Mujat, R.C. Chan, B. Cense, B.H. Park, C. Joo, T. Akkin, T.C. Chen, and J.F. de Boer, "Retinal nerve fiber layer thickness map determined from optical coherence tomography images," Opt. Express **13,** 9480-9491 (2005).
27. W. Drexler, U. Morgner, R.K. Ghanta, F.X. Kartner, J.S. Schuman, and J.G. Fujimoto, "Ultrahigh-resolution ophthalmic optical coherence tomography," Nat. Med. **7,** 502-507 (2001).

#78463 - $15.00 USD Received 22 December 2006; revised 13 February 2007; accepted 15 February 2007

1. Introduction

Optical coherence tomography (OCT) [1, 2] is a technique for non-invasive three-dimensional imaging of turbid media, such as biological tissue. Polarization-sensitive OCT (PS-OCT) can measure the birefringence and optic axis of biological tissue [3-7]. Linear birefringence is an optical property that describes the difference in index of refraction for light polarized along and perpendicular to the optic axis. Birefringence occurs in neatly oriented fibers of biological tissue, such as collagen, tooth enamel, and the retinal nerve fiber layer. *In vivo* time-domain ophthalmic PS-OCT measurements around the optic nerve head of up to five healthy young volunteers not only have shown the well known variation of the human retinal nerve fiber layer thickness, but also more importantly have demonstrated a variation of the birefringence around the optic nerve head [8-10]. Using a different method, the same observation was made by Huang *et al* [11]. Specifically for the retinal nerve fiber layer, the same group suggested that nerve fiber layer birefringence is proportional to the microtubule density [12]. A birefringence measurement may therefore be used to analyze microtubule density, which may lead to a better understanding of the pathophysiology of the nerve fiber layer architecture changes that occur in glaucoma (the world's second leading cause of blindness). Since microtubules are 25 nm thin structures [12], sub-wavelength information on the microtubules could be acquired with PS-OCT, even though the axial and lateral resolutions of the technique are orders of magnitude lower.

The first *in vivo* human Spectral/Fourier domain OCT (SD-OCT) images were reported by Wojtkowski *et al* [13]. The sensitivity advantage of SD-OCT over time-domain OCT can be used either to shorten the acquisition time by a factor of 150 or to improve the signal-to-noise ratio (SNR) [14-17]. Yasuno *et al*. reported measurements on human skin *in vitro* using a polarization sensitive SD-OCT (PS-SD-OCT) system [18]. PS-SD-OCT systems for *in vivo* applications have only been developed recently. In 2005, we demonstrated PS-SD-OCT systems at 1310 nm [19] and 830 nm [10] that used a polarizing beam splitter in the detection arm to separate the two orthogonal states on two line scan cameras. Recently, Götzinger *et al*. demonstrated a PS-SD-OCT system for ophthalmic applications that used two separate spectrometers in the detection arm [20]. Yamanari *et al*. demonstrated a fiber-based PS-SD-OCT system at 840 nm for non-ophthalmic applications [21]. So far only qualitative determination of nerve fiber birefringence has been demonstrated with PS-SD-OCT systems, except for our earlier work that, however, was sensitive to a linear birefringence artifact attributed to incorrect mapping of the orthogonally polarized interference spectra to wavevector [10, 19]. In this paper, we demonstrate an ophthalmic system at 840 nm that uses an elegant polarization-sensitive spectrometer design using a single line scan camera. In such a configuration, only one camera has to be synchronized with other components in the system, simplifying the design. Measurements on one healthy young volunteer were used to demonstrate that incorrect mapping has been resolved and that the quantification of tissue birefringence is equal to that determined with our earlier time domain system.

2. Materials and Method

An SD-OCT system [22] was made polarization-sensitive by adding a polarization modulator (New Focus, model 4102) in the source arm and a Wollaston prism in between the grating and the lens of the spectrometer in the detection arm (Fig.1).

A high-power superluminescent diode (SLD-371-HP, Superlum, λ_0 = 840 nm, $\Delta\lambda_{FWHM}$ = 50 nm) was isolated by means of a broadband isolator (OFR), and at the exit of the isolator the light was linearly polarized. A PC with dual Intel Xeon processors and a National Instrument I/O board (NI6733) generated the driving waveform for the polarization modulator (New Focus), which was positioned directly after the isolator.

#78463 - $15.00 USD Received 22 December 2006; revised 13 February 2007; accepted 15 February 2007

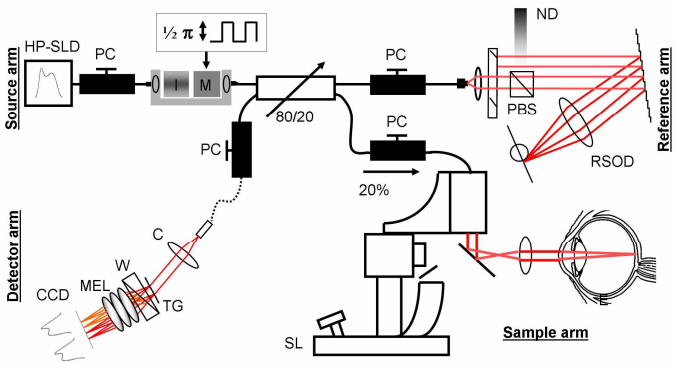

Fig. 1. Measurement setup for polarization-sensitive spectral-domain optical coherence tomography. Light from a broadband source (HP-SLD) was coupled through an isolator (I) and modulated at 29,300 Hz with a bulk polarization modulator (M). An 80/20 fiber coupler distributed the modulated light over sample and reference arms. The retina was scanned with a slit lamp (SL) based retinal scanner, and the reference arm consisted of a rapid scanning delay line (RSOD), employed with a polarizing beam splitter (PBS) to ensure a constant polarization state returning from the RSOD, and a variable neutral density filter (ND) for attenuation. In the detection arm, interference fringes were detected with a high-speed polarization-sensitive spectrometer. Light was collimated (C_f = 100 mm) and diffracted with a transmission grating (TG, 1200 lines/mm) after which a photographic multi-element lens (MEL; f = 105 mm) focused the spectra on a line scan CCD camera (CCD). A calcite Wollaston beam splitter (W) in the detection path directed orthogonal polarization components to the same camera, which was synchronized with the polarization modulator in the source arm. Polarization controllers (PC) were used to fine-tune the polarization state of the light.

The waveform was amplified with a high voltage amplifier and sent to the modulator. The waveform consisted of a square wave with a maximum frequency of 29,300 Hz, resulting in two different polarization states generated by the modulator that were 90° separate in a Poincaré sphere representation [6]. The modulation frequency could be slowed down arbitrarily to increase the measurement sensitivity as desired by increasing the integration time of the line scan camera accordingly. The polarization modulator was synchronized with the line scan camera in the detection arm such that alternate A-lines were acquired with two different input polarization states. By means of frame-triggering, each B-scan, or frame, was synchronized with the fast scanning axis of the slit lamp apparatus. A second National Instruments I/O board (NI6110) generated the waveforms for the galvanometers.

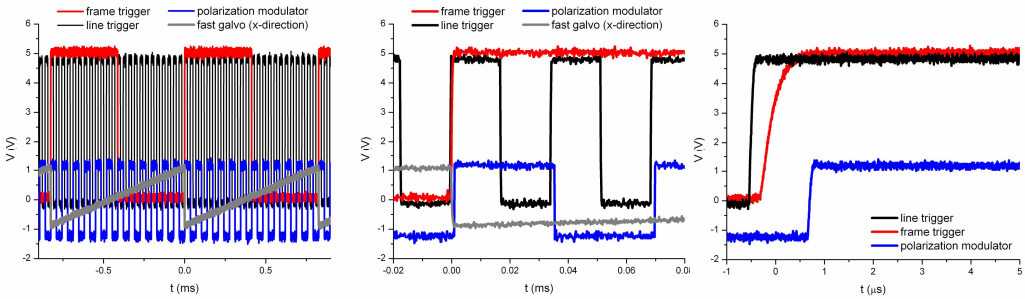

Fig. 2. Synchronized trigger waveforms for the line scan cameras (line trigger, frame trigger) and driving waveforms for the polarization modulator and fast galvanometer. From left to right, graphs are shown at a shortened time scale. For clarity, only 20 spectra were grabbed per scan. In reality, 1000 spectra were recorded per cycle of the fast galvanometer. A time delay between the starting points of the different waveforms (right plot) was created to compensate for delays in the line scan cameras and the polarization modulator.

#78463 - $15.00 USD Received 22 December 2006; revised 13 February 2007; accepted 15 February 2007

In the example of Fig. 2, the trigger and driving waveforms are shown for a configuration where only 20 A-lines were acquired for one image. The driving waveform for the fast galvanometer increased linearly and started simultaneously with the up-going flank of the frame trigger waveform. Within this frame, 20 pulses were generated to trigger the acquisition of a spectrum at every up-going flank. Since there was an internal delay in the camera of 2 μs, and a 1 μs delay in the polarization modulator, the polarization modulator signal was delayed in software by approximately 1 μs.

An 80/20 fiber coupler sent 80% of the power to the reference arm. A rapid scanning delay line (RSOD) was equipped with a polarizing beam splitter, ensuring transmission of equal amounts of power through the delay line for both input polarization states. The RSOD was mainly used for second order dispersion compensation and the galvanometer mirror was kept stationary. Light returning from the reference arm interfered with light returning from the sample arm, where a slit lamp was used to image the retina.

Interference spectra were recorded with the polarization-sensitive spectrometer in the detection arm. Light was first collimated and diffracted with a transmission grating (1200 lines per mm, Wasatch Photonics), after which a Nikon lens (f = 105 mm) was used to focus the light onto the line scan CCD camera (Basler, 2048 elements of 10 by 10 μm, maximum line frequency 29,300 Hz). A custom made calcite Wollaston prism with a separation angle of six degrees (Karl Lambrecht Corporation) directed both orthogonal states to the same line scan camera, such that the first 1024 pixels were used for the first orthogonal state, while the second state was imaged on the remaining 1024 pixels. The line scan camera was mounted on a five-axis translation/rotation stage (New Focus). When we aligned a system without a Wollaston prism [22], we noticed that the highest efficiency could be obtained when the camera was slightly tilted with respect to the incoming beam. The different wavelengths in the spectrum experienced a different focal length, most likely due to chromatic aberration. A similar approach could not be used here, because a tilt of the camera would lead to a better focus of one spectrum, while simultaneously bringing the second spectrum out of focus. After carefully balancing the foci of the two spectra, we measured the reflection from a mirror in the sample arms at different optical path length differences [23]. In Fig. 3, the intensities for the two orthogonal channels, H and V, are given as functions of depth. Data was fitted with a least-squares linear fit and the sensitivity decay of both plots was equal to 10±1 dB/mm. Both plots overlap to within 0.2 dB, which demonstrates that the two spectra were equally well focused.

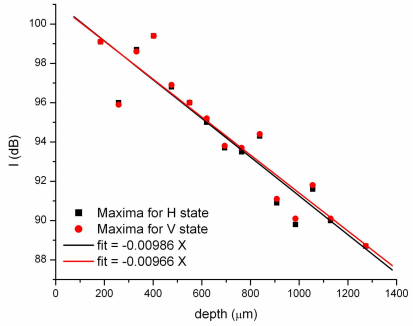

Fig. 3. Measurements on a mirror in the sample arm at different optical path length differences. Measurements were taken for the horizontal (H) polarization channel and vertical (V) polarization channel. Red and black lines represent linear fits to the data.

Orthogonally polarized spectra were recorded simultaneously and stored to hard disk. In real time, an on-screen frame rate of approximately three frames per second was maintained.

#78463 - $15.00 USD Received 22 December 2006; revised 13 February 2007; accepted 15 February 2007

The polarization state in all arms of the interferometer was optimized using polarization controllers.

The system was equipped with a CCD camera in the slit lamp scanning apparatus that imaged the retina for the positioning of the scans around the optic nerve head. These camera images were not stored to hard disk. Prior to and during data acquisition, information from the CCD camera and the real-time OCT structural intensity display were used to aim the scanning beam through the center of the pupil and to position the scans around the optic nerve head. Furthermore, both imaging modalities were used to focus the beam onto the retina, guaranteeing data with the highest possible SNR.

All experiments were performed under a protocol that adhered to the tenets of the Declaration of Helsinki and met with the approval of the Institutional Review Boards of both the Massachusetts Eye and Ear Infirmary and Massachusetts General Hospital. Since the goal of this study was to demonstrate that a Wollaston based system yields similar results as our earlier time domain polarization-sensitive system, one healthy volunteer was enrolled.

For comparison, the healthy volunteer (a 41-year old Caucasian male) was previously imaged with a polarization-sensitive time-domain system [9] and a two-camera polarization-sensitive spectral-domain system [10]. For this experiment, the power of the light incident on the volunteer's undilated right eye was equal to 515 μW, well below the ANSI standards for safe use of near infrared light [24]. The data set was made with concentric circular scans (12 circular scans of 3000 A-lines each) equidistantly spaced with radii between 1.3 and 2.6 mm. A fixation spot was provided to the right eye to improve the stability of the eye. Data was acquired with an integration time of 33 μs per A-line. This setting was still almost 60 times faster than the time-domain measurement [9], reducing the total measurement time for 12 circular scans from 72 s to 1.2 s.

Using a calibration method with two Fabry-Perot cavities in the source arm, the spectral mapping to wave vector was calibrated such that no birefringence artifacts occurred [25]. In short, the Fabry-Perot cavities in the source arm generated an intensity modulation of the source spectrum that is perfectly periodic in the wave vector domain (k-domain). This perfect periodicity was used to calibrate the mapping of the spectrum to wave vector space for both orthogonal polarization states. The intensity modulation has to be identical in the two polarization channels, and this condition was used to remove the ghost birefringence previously unaccounted for. Two adjacent A-lines made with two different input polarization states were used for a Stokes vectors analysis [5]. By comparing Stokes vectors at the surface of the nerve fiber layer with vectors in depth, the double-pass phase retardation was calculated [6]. By fitting double-pass phase retardation data of the nerve fiber layer with a first-order polynomial, a value for the double-pass phase retardation per unit depth (DPPR/UD) of the nerve fiber layer was obtained. The double-pass phase retardation per unit depth is proportional to the birefringence. The surface Stokes vectors were chosen approximately three pixels (11 μm) below the automatically-detected surface [26]. Moving-average filters were used to reduce the influence of speckle noise. In the horizontal direction we averaged over 60 A-lines, while in the vertical direction we averaged over 3 points, which corresponds to approximately 11 μm in depth. The thickness and birefringence of retinal nerve fiber layer tissue was measured as a function of sector and radius. Each circular scan was divided into 50 sectors of 7.2°. The 50 sectors almost matched the 48 sectors that were analyzed in the time-domain data [9]. However, since we scanned 3000 A-lines per circular scan with SD-OCT compared to 1536 A-lines per time-domain circular scan, the number of A-lines that was averaged to reduce speckle noise was almost two times higher with the current settings. This may have further reduced the influence of speckle noise.

#78463 - $15.00 USD Received 22 December 2006; revised 13 February 2007; accepted 15 February 2007

3. Results

Figure 4 is a structural intensity image that was taken close to the optic nerve head. The image was taken along a circle with a radius of 1.8 mm around the optic nerve head. The image was magnified in the vertical direction (1.89 mm) and a dynamic range of 30.3 dB above the noise floor was gray-scale encoded on a logarithmic scale. Reflections were encoded in black. All retinal layers previously seen with other OCT systems can be seen here as well [27]. Figure 5 is a similar image at a radius of 2.5 mm centered on the optic nerve head. The upper layer is the nerve fiber layer, which is thickest superior and inferior to the optic nerve head. Although the nerve fiber layer becomes thinner at a larger scanning radius, the retinal nerve fiber layer thickness is always greater superior and inferior to the optic nerve head, regardless of scan radius. The sinusoidal pattern at which the retina is displayed is most likely caused by a tilt of the eye with respect to the scanning beam. The images were not realigned during post-processing.

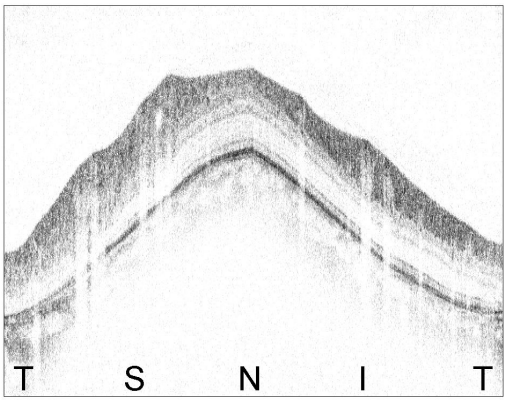

Fig. 4. Structural intensity image taken with a circular scan (r = 1.84 mm, length x height of scan = 11.6 x 1.89 mm, magnified in the vertical direction for clarity) around the optic nerve head. T (temporal); S (superior); N (nasal); I (inferior). The upper layer is the nerve fiber layer. It is thickest superior (S) and inferior (I) to the optic nerve head.

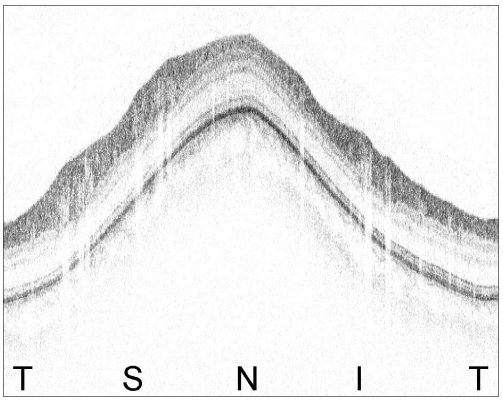

Fig. 5: Circular B-scan taken further away from the optic nerve head (r = 2.49 mm, length x height of scan = 15.6 x 1.89 mm, magnified in vertical direction for clarity). The nerve fiber layer is thinner at this location. However, as in Fig. 4, the nerve fiber layer is still thicker superior (S) and inferior (I) to the optic nerve head.

In Fig. 6 (left), we determined the thickness and birefringence of 60 averaged A-lines of a sector in the thinner temporal part of Fig. 4. Starting from the surface, the plot displays the

#78463 - $15.00 USD Received 22 December 2006; revised 13 February 2007; accepted 15 February 2007

intensity (on a logarithmic scale) and DPPR/UD. The bottom of the nerve fiber layer was estimated by an operator based on a change in the reflectivity and a change in slope of the DPPR [10]. A vertical line in the plot marks this position. The double-pass phase retardation curve that belonged to the nerve fiber layer was fit with a first-order polynomial. A similar analysis was done for a sector in the thicker inferior part (Fig. 6 right).

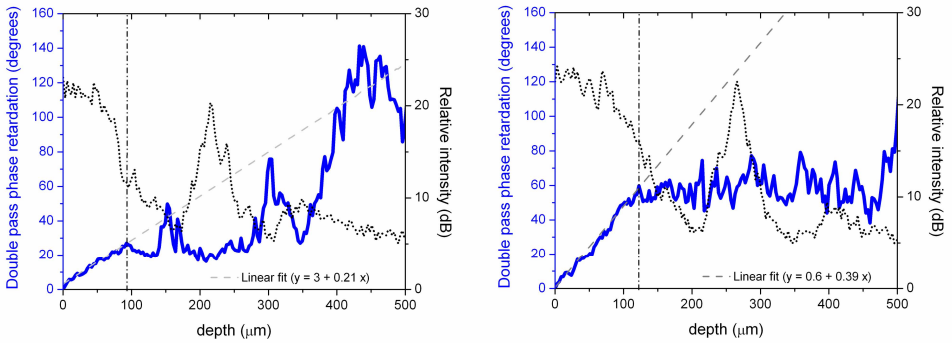

Fig. 6. Retinal nerve fiber layer thickness (black dotted) and double-pass phase retardation (blue solid) measurements in sectors temporal (left) and inferior (right) to the optic nerve head. Double-pass phase retardation data belonging to the retinal nerve fiber layer was fit with a first-order polynomial. The slope of this fit – proportional to the birefringence - is given in the lower right corner.

The blood vessels (white columns in Figs. 4 and 5) influenced the double-pass phase retardation calculation. In a similar analysis that was performed for time-domain PS-OCT data, it was already noticed that blood vessels distorted the calculation, yielding lower double-pass phase retardation values [9]. As a quantitative analysis was not presented before, we demonstrate in Figs. 7 and 8 how the inclusion of blood vessel A-lines can affect a double-pass phase retardation measurement. From these results it should be clear why A-lines going through a blood vessel were not included in our data presented in Fig. 9. In Fig. 7, vertical red lines indicate where this particular measurement was taken. Notice that both images were realigned with respect to the retinal surface. The retardation image was gray-scale encoded; black pixels indicate a double-pass phase retardation of 0° while white pixels represent a retardation of 90°. Since the combination of two A-lines resulted in one double-pass phase retardation calculation, the number of depth profiles in the birefringence image is reduced to 1500. In the phase retardation image, the location of blood vessels can be correlated to black columns, indicating low values for double-pass phase retardation. We started averaging from the right of the left red line with the first 10 A-lines only, not including the blood vessel. The resulting DPPR/UD value that resulted from a fit through the green data set (Fig. 8) represented a value of 0.31 degrees/μm, a number that is similar to measurements performed earlier at this location [9]. The same results were obtained when we use the first 20 and 30 A-lines. However, when A-lines that went through the blood vessel (magenta, yellow and beige curves) were included, the double-pass phase retardation decreased. A first-order polynomial fit through these data points yielded slopes that were significantly lower, up to 30% below the value for the actual birefringent retinal nerve fiber layer tissue.

#78463 - $15.00 USD Received 22 December 2006; revised 13 February 2007; accepted 15 February 2007

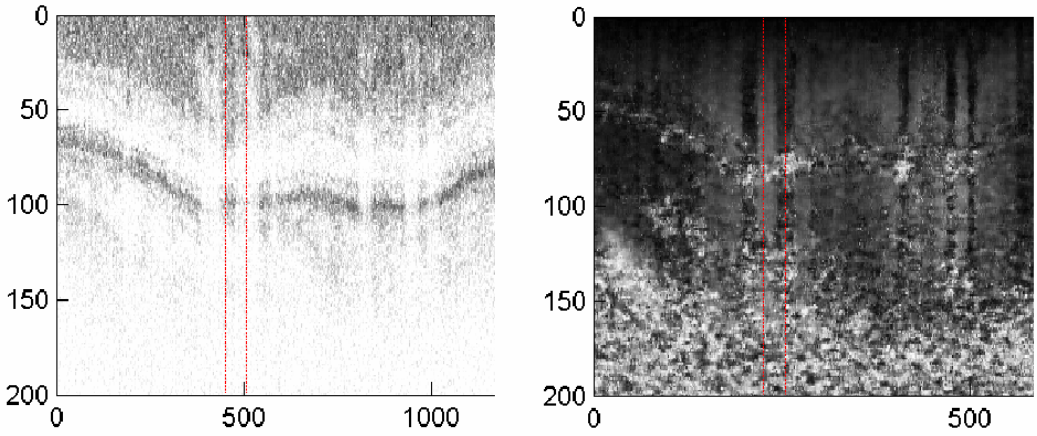

Fig. 7. Structural intensity (left) and phase retardation (right) images, realigned with respect to the retinal surface. Both panels only display the first ~1200 A-lines of the B-scan in and around a blood vessel for clarity. The red lines indicate the sector over which the double-pass phase retardation calculation was averaged. The blood vessel is located in the right part of the sector. Units on the y-axis represent pixels and the 200 pixels cover a distance of approximately 740 µm. In width, the displayed part of the scan measures ~4.6 mm.

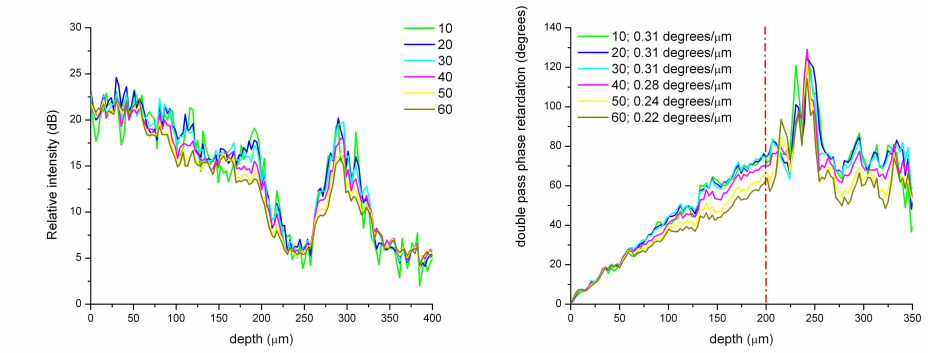

Fig. 8. Intensity (left) and double-pass phase retardation plots (right) not including the blood vessel (green, blue, and light blue curves) are given, as well as plots that include the blood vessel (other curves). The red dash-dotted line roughly indicates the lower part of the nerve fiber layer. This location is found by combining the information per curve using both plots. The higher double-pass phase retardation values directly below the nerve fiber layer are caused by a lack of signal.

In Fig. 9, both the thickness (left) and DPPR/UD (right) are displayed as a function of sector, or position around the optic nerve head. Although 12 circular scans were made around the optic nerve head, only 9 of them were suitable for analysis, since the three innermost scans touched the optic disc edge, indicating that the circular scans were not exactly centered. In the left figure, the different scan radii for each circular scan were represented by different colors. Highest nerve fiber layer thickness values occurred inferior and superior to the optic nerve head. Missing values were caused by sectors that were completely occupied by blood vessels. Values for the thickness and DPPR/UD were determined for sectors with 5 or more A-lines available for analysis (see data in Fig. 8). On

#78463 - $15.00 USD Received 22 December 2006; revised 13 February 2007; accepted 15 February 2007

the right, the DPPR/UD measurements at different radii are displayed. Measurements originating from one circular scan were labeled with the same symbol. The red line represents the average value for each sector, while error bars indicate the standard error [9]. Similar to previous measurements, highest thickness and DPPR/UD values were found superior and inferior to the optic nerve head, while the spread in data points was highest nasal to the optic nerve head [9]. The higher deviation in these nasal sectors is most likely caused by a less reliable analysis in a thinner nerve fiber layer.

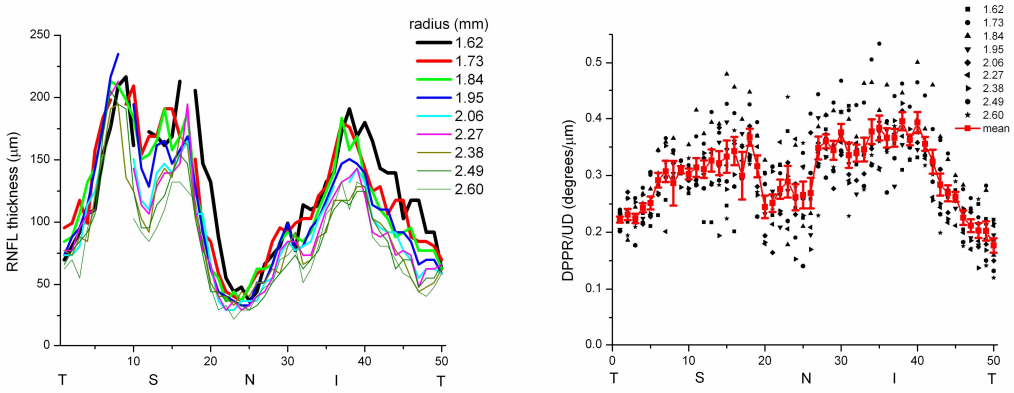

Fig. 9. (left) Retinal nerve fiber layer thickness as a function of distance and relative position to the optic nerve head. (right). DPPR/UD values of each sector displayed as a function of distance (symbol) and relative position (x-axis) to the optic nerve head. Mean values per sector are connected with a red line. Error bars indicate the standard error.

From the left plot in Fig. 9, we can determine that the thickness varies between ~25 µm and 225 µm. On the right, the highest DPPR/UD values occur inferiorly at approximately 0.40 degrees/µm, while the lowest values are found temporally at approximately 0.18 degrees/µm. These values are equivalent to a birefringence of $4.8 \cdot 10^{-4}$ and $2.2 \cdot 10^{-4}$ respectively, measured at 840 nm.

4. Discussion

The trends that we can see in these measurements are similar to the trends in measurements that were performed earlier with a time-domain PS-OCT system [9]. There are slight differences in the thickness plot. Here, the maximum thickness was approximately 225 µm, while earlier measurements indicate a maximum value of 250 µm. This difference can be explained by the fact that the circular scans were not exactly centered at the optic nerve head. As a result, the inner three data sets were not analyzed.

The DPPR/UD values of the earlier data set varied between ~0.1 and 0.4 degrees/µm. Here, values are less variable and vary between 0.18 and 0.4 degrees/µm. There is no clear explanation for this difference. Although the time-domain data had a higher dynamic range (~35 dB vs. ~32 dB), there were fewer A-lines available for speckle averaging. Double pass phase retardation data was therefore sometimes more influenced by speckle noise. Sectors in thin nerve fiber layer are less reliable because of fewer data points. The nasal sectors in particular were challenging to analyze, not only because of the thickness of the tissue, but also because the boundary between the nerve fiber layer and the ganglion cell layer was particularly difficult to judge here. An automatic detection method that uses the intensity information [26] and the double pass phase retardation information, would make the analysis more objective.

#78463 - $15.00 USD Received 22 December 2006; revised 13 February 2007; accepted 15 February 2007

5. Conclusion

PS-SD-OCT can be performed using a spectrometer configuration with a single line scan camera and a Wollaston prism. In such a configuration, only one camera has to be synchronized with other components in the system, simplifying the design. Using concentric circular scans around the optic nerve head of a 41 year old Caucasian healthy volunteer, structural intensity images were made and polarization-sensitive data was acquired. Data from blood vessels was omitted in the polarization analysis. The acquired data sets showed variations in retinal thickness and DPPR/UD that were similar to data from the same volunteer taken with a time-domain polarization-sensitive system. The DPPR/UD varied between 0.18 and 0.4 degrees/μm, equivalent to a birefringence of $2.2 \cdot 10^{-4}$ and $4.8 \cdot 10^{-4}$ respectively, measured at 840 nm.

Acknowledgments

This research was supported in part by research grants from the National Institutes of Health (R01 EY014975) and the Department of Defense (F4 9620-01-1-0014).

#78463 - $15.00 USD Received 22 December 2006; revised 13 February 2007; accepted 15 February 2007